Enhanced thermoelectric performance by resonant vibrational mode-selective density-of-states distortions

Shantonio W. Birch[1a)] and Kevin P. Pipe[1,2,]

[1]Department of Mechanical Engineering, University of Michigan, Ann Arbor, MI 48109-2125

[2]Department of Electrical Engineering and Computer Science, University of Michigan, Ann Arbor, MI 48109-2122

[a)] Author to whom correspondence should be addressed: swbirch@umich.edu

Electronic Supplementary Information (ESI)

ESI Note 1 – Numerical modeling of the unperturbed material's DOS.

ESI Note 2 – Numerical modeling of mode-selective density-of-states distortion.

ESI Note 3 – Polaronic origins of kink-like features at the top of the HOMO band.

ESI Note 4 – Photo-optimization of the Seebeck coefficient and electrical conductivity.

ESI Note 5 – Photoexcitation of Holstein small polarons versus PJT polarons.

ESI Note 1 – Numerical modeling of the unperturbed material's DOS.

In modeling the unperturbed DOS, we consider a phenomenological broadening of the DOS that is set by the lifetime broadening of electronic states measured by the temperature-dependent narrowing of the FWHM HOMO dispersion [c.f. Eq. (6) of the main manuscript]. Here, we show justification of this approximation by comparing the DOS resulting from applying this phenomenological broadening of the electronic states with the DOS calculated by taking into account the explicit effects of the static as well as the dynamic (phenomenological broadening) components of thermal disorder, as was done in ref.[1]
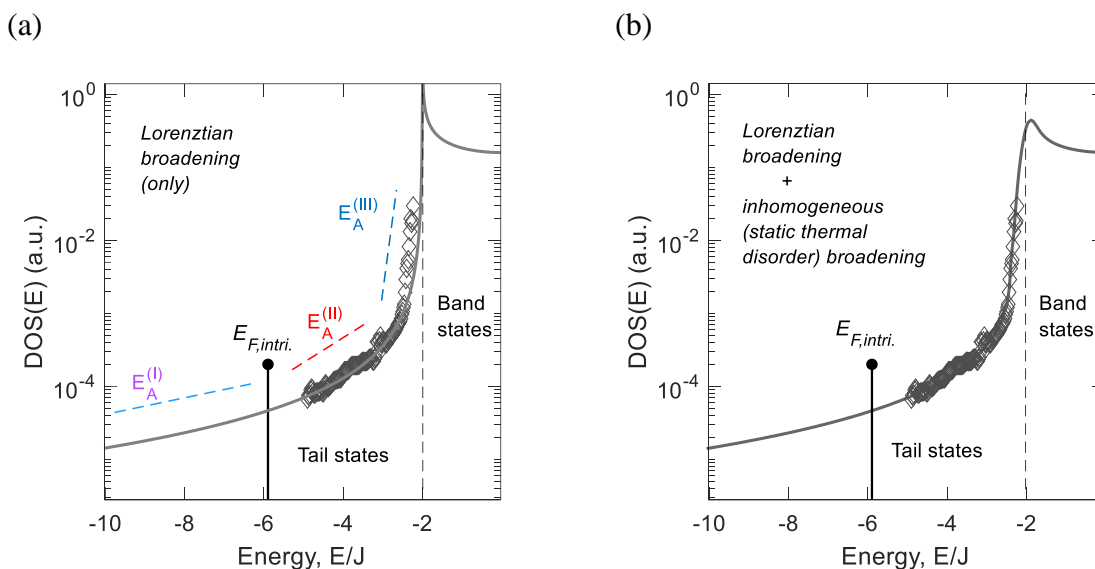
(a)

(b)

Fig. S1. Plot of the DOS showing replication on the biexponential energy dependence of the DOS tail measured in a soft organic material (i.e., rubrene) having characteristic activation energies E_A as those reported in ref.[1] Similar biexponential energy dependence of the DOS tail has been measured in other soft organic materials and amorphous wide bandgap inorganic materials.[2-5] Calculations were performed at room temperature using similar parameters as those used for the case when IR light is off in Fig. 1 of the main manuscript. The diamond markers represent experimental data for the DOS taken from ref.[2] We note that while the origin of the biexponential energy dependence of the DOS tail is likely the result of more complicated interactions that involves the coupling of valence carriers to low-frequency intermolecular vibrations (not considered in the context of mode-selective vibrations discussed in this work), a phenomenological broadening (associated with a Lorentzian component of the FWHM of the HOMO dispersion)[1] is shown in Fig. S1 (a) to give an accurate representation of the experimentally measured DOS before IR light is applied. The effects of the static contribution to thermal disorder on the behavior of the DOS tail, in particular, is shown in Fig. S1 (b) to not appreciably affect the bi-exponential energy dependence of the DOS and thus can be neglected without loss of generality. Note that the presence of the static contribution to thermal disorder is likely to smear out some resonant features in the DOS and therefore could be detrimental to power factor enhancements in tail states. This effect is, however, more likely to affect states near the HOMO band edge (E_{HOMO}) rather than states near the intrinsic Fermi level position, which as shown in the figure is farther away from E_{HOMO}.

ESI Note 2 – Numerical modeling of mode-selective density-of-states distortion.

In modeling the effects of mode-selective density-of-states distortions, we consider the continued fraction method developed in ref.,[6-13] and described in Eq. (3) to (5) of the main manuscript. This method is particularly beneficial as it provides a simple yet numerically exact means for simulating the effects of mode-selective vibrations on creating Dirac-delta-like DOS distortions,[6-8] starting from a representative model of the unperturbed DOS.[9-11] Furthermore, since it preserves the complex interplay between the charge carrier dynamics and the dynamics of their surrounding lattice displacements,[7,11] this framework also allows for the dispersion of the intramolecular vibration mode to be approximated by taking into account higher-order terms in the continued fraction expansion of Eq. (8) (in the main manuscript).[11] Note that while the continued fraction expansion allows us to treat the effects of electron-phonon scattering, we do not account for the effects of phonon-phonon scattering,[14,15] which are likely to not have significant impacts on the TE properties calculations performed in this work due to inherently short phonon mean-free paths that are traditionally measured in this material class.[16-18]

ESI Note 3 – Polaronic origins of kink-like features at the top of the HOMO band.

A distinguishing feature of the mode-selective redistribution of valence carriers is the emergence of a kink-like feature at the top of the HOMO band,[19,20] as recently measured by ultraviolet ARPES measures of the valence dispersion of rubrene.[20] The emergence of this feature has been previously ascribed to the coupling of valence carriers with low-frequency intermolecular vibration having characteristic frequencies of ~10's meV.[20] In Fig. S2, we show that a similar feature can occur by the coupling of valence carriers to the high-frequency intramolecular C-C stretching vibration examined in this work. This effect is exemplified for the case when the rotating wave approximation (RWA) (Fig. S2 (a) and (b)) is invoked to model the mode-selective redistribution of valence carriers as well as for the case when the RWA is not invoked (termed the non-RWA solution). Throughout this work, the more realistic non-RWA solution is used to model the effects of vibrational mode-selective DOS distortions (Fig. S2 (c) and (d)) .
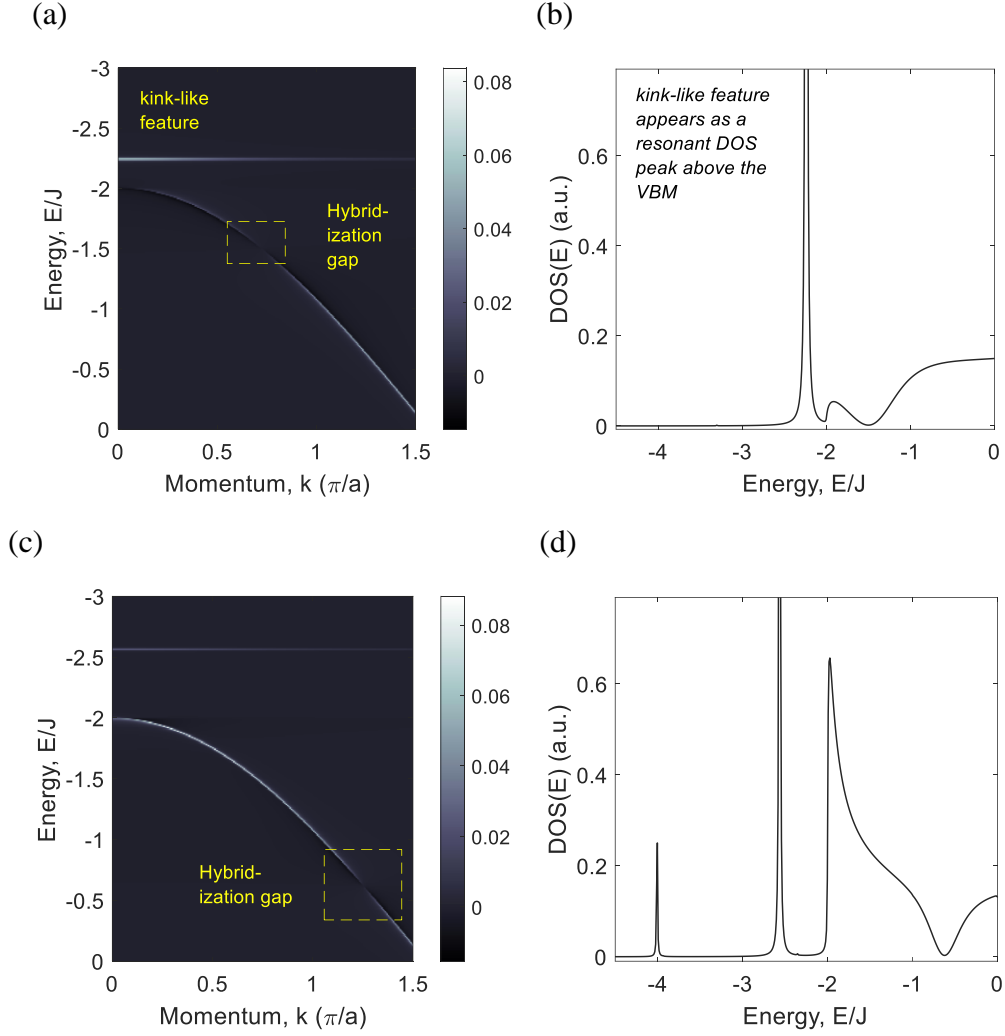
(a)

(b)

(c)

(d)

Fig. S2. Spectral density function $A(k,E)$ and DOS of the modelled material system for the case when (a)-(b) the rotating wave approximation is taken to model the effects of mode-selective vibration and (c)-(d) the case when the rotating wave approximation is not taken (the non-RWA solution). It is important to highlight that while multiple kink-like features are shown to occurs in the plot of $A(k,E)$ corresponding to calculations of $DOS(E)$ carried out for $N_{ph} = 1$ in the main manuscript (see Fig. 2 (a) and S2 (c)-(d)), a single feature is shown to occur under the rotating wave approximation. While unrealistic, this RWA solution for Dirac-delta-like tail states formation can be approached under very specific experimental conditions described elsewhere.[6-8] Furthermore, because molecular vibrations having characteristically larger frequencies than the intermolecular vibrations are used to resonantly perturb band states, the kink-like feature appearing at the top of the band edge is more displaced from the unperturbed valence band edge than the one reported in ref.[20]

4

ESI Note 4 – Photo-optimization of the Seebeck coefficient and electrical conductivity.

The largest enhancement in PF within a particular branch of the vibrational energy state diagram [Fig. 2 (b)] is shown to occur as a result of a general class of $type-v_{n\to n+2}$ electronic transitions that is interpreted to proceed by the pseudo-Jahn-Teller (PJT) effect. The power factor for a particular $type-v_{n\to n+2}$ transition is maximized for the values of N_{ph} corresponding to when a resonant DOS peak is placed approximately $\omega_0/2+2.4k_BT$ from any one of the bifurcation points (shown in Fig. 2 (b)) and the Fermi level is ~$2.4k_BT$ from these displaced DOS peaks. For these values of N_{ph} and E_F, the resonant enhancement of the thermoelectric PF is shown to occur due to the creation of new transport edges in the tail distribution of states, which causes S and σ to be optimized as if dopants were added to shift the Fermi level towards the valence band edge of the unperturbed electronic system. This modulation of the behaviors of S and σ is shown in Fig. S3 (a) and (b) for the cases when the Fermi level is positioned at the center of the bifurcation gaps [shown in Fig. 2 (b)], and in Fig. S3 (c) and (d) when the Fermi level is positioned approximately $-2.4k_BT$ from the center of each branch of the vibrational state energy diagram (i.e., where the asymmetry in $\sigma(E)|_{E_F}$, and thus PF is maximized).
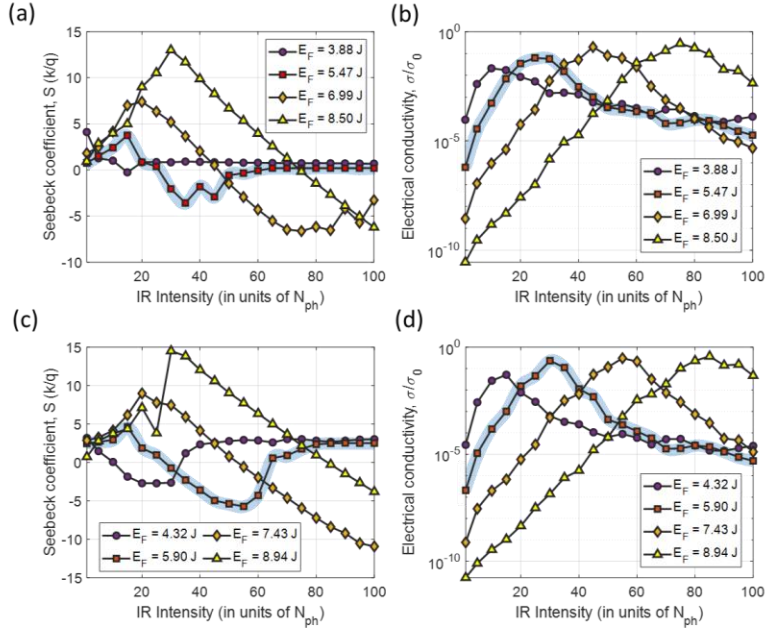
Fig. S3 (a)-(b) Evolution of the thermoelectric coefficients (i.e., S and σ) as the IR intensity is increased to vary a DOS peak across all four of bifurcation points studied in this work. Most notably, the Seebeck coefficient is shown to change signs multiple times from positive to negative as the IR intensity is increased to promote the redistribution carriers from band states to tail states, indicating the onset of ambipolar thermoelectric characteristics as N_{ph} is tuned to vary a resonant DOS peak above or below the bifurcation points (where E_F is fixed). This complexity of carriers being added either above or below the Fermi level (and thus contributing either positively or negatively to the Seebeck coefficient) for various values of N_{ph} leads to the general nonlinear relationship shown in Fig. 3 (b) and Fig. S3 (a) and Fig. S3 (c). Complementary plots for S and σ when the Fermi level is fixed at its optimal position (i.e., when the Fermi level is positioned approximately $-2.4k_BT$ from the center of each branch of the vibrational state energy diagram) are provided in Fig. S3 (c)-(d).

ESI Note 5 - Photoexcitation of Holstein small polarons versus PJT polarons.

Instead of allowing for the preferential redistribution of carriers into a non-equilibrium distribution of excited states (as is considered throughout this work), we can simulate the effects of the "natural" redistribution of valence carriers across all allowed vibronic transitions (i.e., without any predetermined constraints on which transitions are more favorable) by allowing for the change of variable term in Eq. (7) of the main manuscript ($M_s \rightarrow g_{\omega s}\sqrt{N_{ph} + 1}$) to affect all terms in $g_{\omega s}$ in the continued fraction expansion expression for $\Sigma'(E)$. We note that in the present treatment of vibrational mode-selective DOS distortions considered in the main manuscript, the electronic transition from the new electronic ground state to the first excited state is assumed to be a favorable transition, as is typically the case for any material system. The described modification in the modeling of the other $g_{\omega s}$ terms in Eq. (7), on the other hand, amounts to treating the effects of Holstein small polarons, which give rise to the conventional ladder-like "filling" of the excited states,[6-11] in addition to a similar lowering of the electronic ground state energy as described in the main manuscript. However, as the DOS peaks on opposite sides of the Fermi window can be shown in Fig. S4 to progressively get further and further apart from each other for the Holstein small polaron scenario, instead of converging (as they do for the PJT scenario described in the main manuscript), asymmetries in the energy distribution of conducting carriers are not maximized when T = 300 K. This in turn leads to suboptimal power factor enhancements for a corresponding value of N_{ph} that places the resonant DOS peak within the intrinsic Fermi window for the Holstein small polaron scenario when compared to power factor enhancements that proceeds by the resonant intramolecular four-step process described in the main manuscript (Fig. S5).
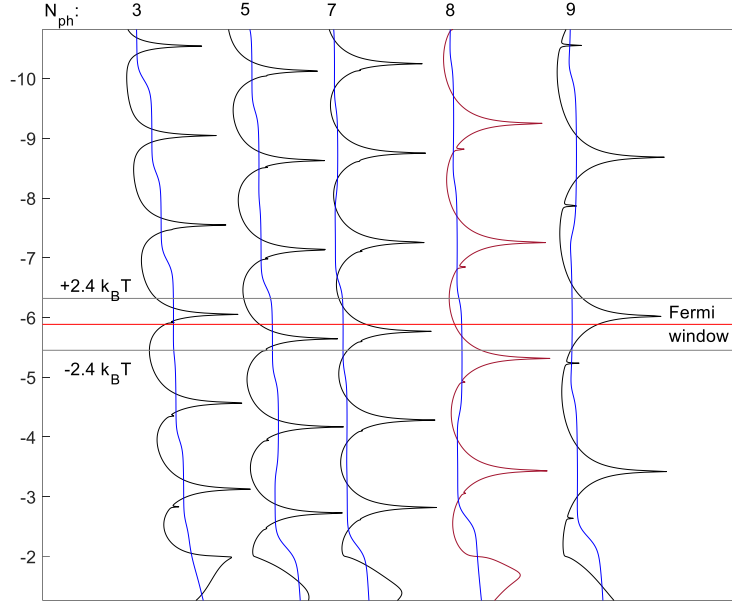
Fig. S4 Predicted modifications of $DOS(E)$ (black lines) and $\mu(E_F)$ (blue lines) within the intrinsic Fermi window as N_{ph} is increased to augment the coupling of valence carriers to C-C stretching vibrations to create Holstein small polarons. While sharp DOS peaks emerge within the Fermi window region corresponding to the Holstein small polaron problem, the spacing between DOS peak on opposite sides of the Fermi window are shown to progressively widen instead of converging, causing $\mu(E_F)$ to remain virtually unchanged (i.e., a constant) within the Fermi window. As a consequence, the asymmetries in the energy distribution of conducting carriers are not maximized.
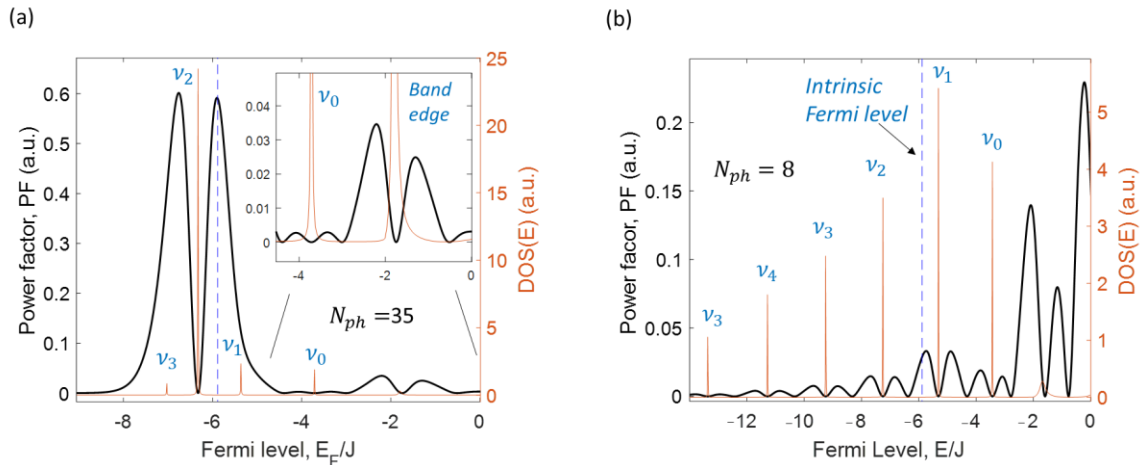

Fig. S5 Predicted thermoelectric PF for a PJT polaron versus a Holstein small polaron. Resonant power factor enhancement via (a) the resonant four-step intramolecular charge transfer process (which involves the formation of PJT polarons) versus (b) the conventional Holstein small polaron process. Calculations for the plots in Fig. S5 (a) were performed for $N_{ph}=35$, while calculations for the plots in Fig. S5 (b) were performed for $N_{ph}=8$. The lower value of N_{ph} needed to achieve a shifting of the vibrations state energies to place a resonant DOS peak at the intrinsic Fermi level position indicated in the figures is notable. The predicted PF enhancement for the Holstein small polaron is shown to be lower than that predicted for a PJT polaron at the same Fermi level position (vertical blue dashed line). Furthermore, unlike DOS peak formation via the resonant four-step intramolecular charge transfer process described in the main manuscript, PF enhancements by Holstein small polaron formation lead to progressively worse room temperature thermoelectric power factor as N_{ph} is increased.

References

1. S. W. Birch and K. P. Pipe, *Journal of Applied Physics*, 2022, 131, 135104.
2. C. Krellner, S. Haas, C. Goldmann, K. P. Pernstich, D. J. Gundlach and B. Batlogg, *Physical Review B*, 2007, 75, 245115.
3. W. L. Kalb, S. Haas, C. Krellner, T. Mathis and B. Batlogg, *Physical Review B*, 2010, 81, 155315.
4. D. Monroe and M. A. Kastner, *Physical Review B*, 1986, 33, 8881–8884.
5. F. Djamdji, P. LeComber, R. Schumacher, P. Thomas and K.Weber, *Journal of Non-Crystalline Solids*, 1987, 97-98, 543–546.
6. S. Swain, Journal of Physics A: Mathematical, Nuclear and General, 1973, 6, 192–204.
7. M. Cini and A. D'Andrea, *Journal of Physics C: Solid State Physics*, 1988, 21, 193–235.
8. A. D'Andrea, *Physical Review A*, 1989, 39, 5143–5152.
9. J. Ranninger, *Physical Review B*, 1993, 48, 13166–13169.
10. S. Ciuchi, F. de Pasquale and D. Feinberg, *Europhysics Letters (EPL)*, 1995, 30, 151–156.
11. S. Ciuchi, F. de Pasquale, S. Fratini and D. Feinberg, *Physical Review B*, 1997, 56, 4494–4512.
12. S. Ciuchi and S. Fratini, *Physical Review Letters*, 2011, 106, 1–4.
13. S. Ciuchi, R. C. Hatch, H. Höchst, C. Faber, X. Blase and S. Fratini, *Physical Review Letters*, 2012, 108, 1–5.
14. H. Ma, C. Li, Y. Ma, H. Wang, Z. W. Rouse, Z. Zhang, C. Slebodnick, A. Alatas, S. P. Baker, J. J. Urban and Z. Tian, *Phys. Rev. Lett.*, 2019, 123, 155901.
15. A. C. Ferreira, S. Paofai, A. Létoublon, J. Ollivier, S. Raymond, B. Hehlen, B. Rufflé, S. Cordier, C. Katan, J. Even and P. Bourges, *Communications Physics*, 2020, 3, 48
16. J. R. Olson, K. A. Topp and R. O. Pohl, *Science*, 1993, 259, 1145–1148.
17. Y. Okada, M. Uno, Y. Nakazawa, K. Sasai, K. Matsukawa, M. Yoshimura, Y. Kitaoka, Y. Mori and J. Takeya, *Physical Review B*, 2011, 83, 113305.
18. Y. Okada, M. Uno, Y. Nakazawa, K. Sasai, K. Matsukawa, M. Yoshimura, Y. Kitaoka, Y. Mori and J. Takeya, *Physical Review B*, 2011, 83, 113305.
19. Y. Nakayama, S. Kera and N. Ueno, *Journal of Materials Chemistry C*, 2020, 8, 9090–9132.
20. F. Bussolotti, J. Yang, M. Hiramoto, T. Kaji, S. Kera and N. Ueno, *Physical Review B*, 2015, 92, 11510